Polarization Multiplexing Based UOWC Systems Under Bubble Turbulence

Bohua Deng, Jiwei Wang, Zhaoming Wang, Zeyad A. H. Qasem, *Student Member, IEEE*, Qian Li, *Senior Member, IEEE*, Xinke Tang, Chen Chen, *Member, IEEE*, and H. Y. Fu, *Senior Member, IEEE*

***Abstract*—High-speed and turbulence-tolerant transmission links are required to meet the growing demand for underwater optical wireless communication (UOWC). However, most previous works were implemented in statically simulated underwater channels with uniform temperature and salinity gradients irrespective of bubble motion. This paper presents an experimental demonstration of a polarization multiplexing (PolMux) based UOWC system considering bubble-induced turbulence. A theoretical transmission model is built and experiments are carried out to investigate the impact of bubble turbulence on PolMux transmission. The general rules of bubble impairments are summarized by manipulating different bubble flow rates, positions and bubble-effected region thicknesses. Moreover, to mitigate these effects, subchannel pairwise coding is implemented to address the subchannel signal-to-noise-ratio (SNR) imbalance issue, and subcarrier pairwise coding is utilized to overcome the subcarrier SNR imbalance, reaching a sum data rate of 8.58 Gbps. This work evaluates the performance of PolMux-UOWC links in the presence of air bubbles and demonstrates the feasibility of pairwise coding to achieve high-speed transmission in UOWC systems with bubble turbulence.**

***Index Terms*—Bubble turbulence, pairwise coding, polarization multiplexing, underwater optical wireless communication.**

I. Introduction

NOWADAYS, underwater optical wireless communication (UOWC) has been demonstrated to be one of the most promising candidates for ocean exploration, including navigation, monitoring, sensing, and military activities [1]. In the past, underwater communication mainly relied on underwater radio frequency communication (URFC) and underwater acoustic communication (UAC). However, RF waves can be strongly absorbed in the water environment, and there are no technical advantages underwater except that very low frequency can be used in certain submarine communications. Meanwhile, although acoustic waves suffer less attenuation underwater than RF waves, UAC has the weaknesses of multi-path propagation, bulky equipment and limited bandwidth resulting in low data rate (∼ kbps) [1], [2]. Compared with UAC, UOWC has relatively low cost and energy consumption, as well as high modulation bandwidth, which can enable data rate above Gbps [1], [3].

In recent years, researchers have been mainly focused on technologies that can further enlarge the capacity of underwater systems. One of the preferable techniques is polarization multiplexing (PolMux). The polarization state is a natural property of light. Different polarization states of light beams can be harnessed as information carriers for multiplexing, which allows simultaneous transmission of independent signals in two orthogonal polarized states without interference [4], [5]. In addition, spectrally efficient orthogonal frequency division multiplexing (OFDM) with high-order quadrature amplitude modulation (QAM) can also be employed to achieve high transmission capacity. PolMux-OFDM technique has been demonstrated in optical fiber links [6], [7], free space [8], as well as underwater environments [9], [10], which can theoretically double the transmission capacity.

Although PolMux has many advantages as mentioned above, several challenges still hinder the development of high-speed PolMux-UOWC systems. On the one hand, most multi-channel transmission links face the frequency selective problem [11]. More specifically, when OFDM is applied, the high-frequency subcarriers (SCs) might suffer from much more severe power attenuation than the low-frequency SCs. Thus, the overall system performance is limited by the SCs with degraded signal-to-noise-ratio (SNR). To address this issue, one strategy is to use adaptive bit loading [12], [13], which allocates more bits on the low-frequency SCs and less bits on the high-frequency SCs. However, bit loading usually has high complexity due to the requirement of timely SNR feedback from the receiver (Rx) to the transmitter (Tx) and the use of multiple constellations. On the other hand, in different ocean types, the presence of uneven temperature distribution, salinity, and flowing bubbles underwater will cause varying degrees of attenuation along the transmission path [14], [15], [16], [17]. There are multiple

---

Manuscript received 19 December 2022; revised 22 February 2023 and 27 March 2023; accepted 30 March 2023. Date of publication 10 April 2023; date of current version 4 September 2023. This work was supported in part by the National Natural Science Foundation of China under Grant 62271091 and in part by the Shenzhen Technology and Innovation Council under Grant JSGG20210818101404013. *(Corresponding authors: Chen Chen; H. Y. Fu.)*

Bohua Deng and Zhaoming Wang are with the Tsinghua Shenzhen International Graduate School, Tsinghua University, Shenzhen 518055, China (e-mail: dbh21@mails.tsinghua.edu.cn; wangzm19@tsinghua.org.cn).

Jiwei Wang and Chen Chen are with the School of Microelectronics and Communication Engineering, Chongqing University, Chongqing 400044, China (e-mail: 202112021031t@cqu.edu.cn; c.chen@cqu.edu.cn).

Zeyad A. H. Qasem and Qian Li are with the School of Electronic and Computer Engineering, Peking University, Shenzhen 518055, China (e-mail: zeyadqasem@pku.edu.cn; liqian@pkusz.edu.cn).

Xinke Tang is with the Peng Cheng Laboratory (PCL), Shenzhen 518055, China (e-mail: tangxk@pcl.ac.cn).

H. Y. Fu is with the Tsinghua Shenzhen International Graduate School, Tsinghua University, Shenzhen 518055, China, and also with the Peng Cheng Laboratory (PCL), Shenzhen 518055, China (e-mail: hyfu@sz.tsinghua.edu.cn).

Color versions of one or more figures in this article are available at https://doi.org/10.1109/JLT.2023.3265990.

Digital Object Identifier 10.1109/JLT.2023.3265990

factors contributing to bubble generation in the ocean, such as rain, waves, propellers of underwater vehicles, and gases released from the seabed. In these cases, the size and shape of bubbles vary but always have a constant generation flow rate, resulting in a discretized and dynamic bubbles distribution that degrades UOWC system performance. In addition, these bubbles can be stabilized by acquired organic coatings or absorbed particles, which prolong their existence [18], [19]. Therefore, when applying UOWC to real oceanic environments, the impact of bubble-induced turbulence needs to be considered, and bubble characteristics such as flow rate, position and thickness should be comprehensively investigated and potential solutions need to be proposed.

For the PolMux-UOWC system, transmission over the same underwater channel may cause different impacts on two orthogonal polarization light signals. As demonstrated in our work, polarization orthogonality can be disrupted by the bubble channel, thus altering the optical power of two received polarization multiplexed signals. In addition, imperfect system alignment, turbulence, impurities, and fish blocking may lead to polarization state rotation [20], [21], resulting in an SNR imbalance between PolMux subchannels. Therefore, we need methods to mitigate the unbalanced SNR of two subchannels as well as SCs within the OFDM frame.

Pairwise coding (PWC) technique pairs two components with unbalanced SNR to achieve better performance [22]. For optical fiber channels, PWC has been demonstrated to reduce the polarization-dependent loss (PDL) of a coherent PolMux optical transmission [23]. It can also reduce dispersion-induced power fading in intensity-modulated direct-detection (IM-DD) systems [24]. While in [25], PWC assisted data transmission over step-index plastic optical fiber (SI-POF) to improve the BER performance. Besides, PWC with singular value decomposition precoding was used to maximize the overall performance in multiple-input multiple-output (MIMO) optical wireless systems [26].

This work provides novel contributions to UOWC systems in the following aspects. The impairments of bubble-induced turbulence on two orthogonally polarized optical beams are detailly considered based on optical transmission theory and experiments. In the experiments, an adjustable bubble generator is used to emulate the bubble flow underwater, and the influences of varying bubble flow rates, positions and bubble-effected region thickness are investigated. Also, a theoretical bubble-induced system model is provided. In addition, we propose to employ subchannel-PWC (SCH-PWC) to build a robust PolMux-UOWC system against SNR imbalance between two PolMux channels induced by bubbles and compare its performance with subcarrier-PWC (SC-PWC), which is usually adopted to mitigate the system bandwidth limitation. Furthermore, statistical analysis is used to explore the impact of different bubble conditions and data rates on communication performance, from which the most effective encoding methods for different bubble-induced scenarios are discussed. To the best of our knowledge, this is the first work exploring the influence of bubble-induced channels on PolMux transmission and using PWC methods for compensation in both spatial and spectral degrees of freedom.

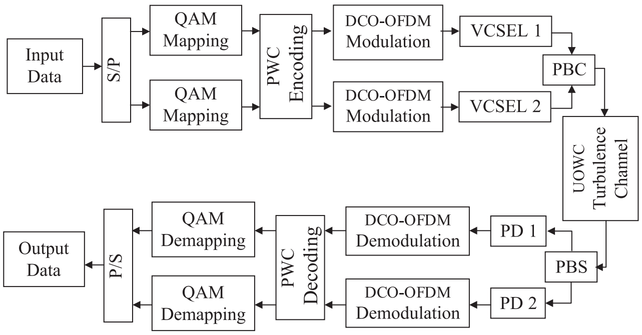

Fig. 1. The block diagram of the bubble induced PolMux-UOWC system.

This experimental demonstration shows the great potential of PWC to realize high-speed communication of UOWC under bubble channels without using any complex offline processing algorithm.

The remainder of this paper is organized as follows. In Section II, we build the bubble-induced PolMux system transmission model and theoretically analyze the different effects of bubbles on two orthogonal-polarized light signals, as well as introduce the coding and decoding process of different PWC schemes. Section III demonstrates the experimental setup of the employed PolMux UOWC system and presents channel and received signal characterization. PWC compensation results are described in Section IV, while conclusions are given in Section V.

II. POLMUX-UOWC UNDER BUBBLE TURBULENCE

A. *System Design*

In order to investigate the characterization of PolMux -based UOWC systems under bubble-induced turbulence, we adopt a typical PolMux-UOWC system. Two serial data streams of independent information for two different users are allocated to light beams with mutually orthogonal polarization states. In addition, a bubble generator is employed to control different bubble channel scenarios. The overall architecture is shown in Fig. 1. At the Tx side, two information streams are first mapped into QAM symbols with modulation order M, followed by PWC encoding and DCO-OFDM modulation. Then, the OFDM frames are modulated on a pair of light sources. Here we use vertical cavity surface emitting lasers (VCSELs) as the transmitters, which can maintain complete polarization control under high frequency modulation [27], [28]. Afterward, a polarization beam combiner (PBC) combines the output emitting beams and forms the final polarization multiplexed transmitted beam. To control the experimental variables, a tunable neutral-density optical filter is adopted in one of the polarization channels to maintain the intensities of two polarized light signals consistent. The beams with two polarization states then propagate through bubble-induced underwater turbulence channel.

To synthesize the general conclusions about the effect of bubbles on signal transmission, four kinds of bubble flow rates (ultra-large, large, medium, and small) controlled by a bubble generator, three different bubble positions (close to Tx, middle and close to Rx) and two bubble-effected region thicknesses (0.07 m and 0.14 m) are mainly set in the experiments. At the Rx side, the beam is divided into two orthogonal polarized lights by a polarization beam splitter (PBS). The two mutually perpendicular polarized optical signals are received by two avalanche photodiodes (APDs) for photoelectric signal conversion, and the electrical signals are connected to two channels of the oscilloscope for simultaneous acquisition. Finally, the received data can be obtained by DCO-OFDM demodulation and the PWC decoding process for polarization degree analysis.

B. Transmission Model

The degree of turbulence in UOWC caused by the random change of salt, turbidity, temperature as well as bubbles in the water medium can be described using fluctuation of the underwater refractive index σ_I^2 [29], which can be calculated by:

$$\sigma_I^2 = \frac{D[I]}{E^2[I]} = \frac{E[I^2] - E^2[I]}{E^2[I]} \tag{1}$$

where *E*[*I*] and *D*[*I*] denote the expected value and the variance of the random variable *I*, respectively.

Light scattering is mainly considered when passing through inhomogeneous mediums such as turbid water. However, as for the bubble channel, the polarization state of the scattered light remains unchanged [30]. This paper mainly considers refraction and reflection due to the change in the refractive index of water and the inner medium of the bubble – air. As a result, the received signals with polarization states *X* and *Y* can be attenuated differently. This phenomenon can be reflected by the difference of the detected optical powers and received SNRs, which will be demonstrated in Section III. Whereas the overall performance of PolMux underwater channel is determined by both channels. As a result, the bubble-induced turbulence will affect the link communication performance. Assume the refractive indexes of the incident medium and the angle of incidence are n_1 and β, and the refractive index of the exit medium and the angle of outgoing are n_2 and γ. According to Fresnel's formula, the complex amplitude coefficients for transmission of polarization states *X* and *Y* can be calculated as

$$\begin{cases} t_X = \frac{2cos\beta sin\gamma}{sin(\beta+\gamma)cos(\beta-\gamma)} = \frac{2n_{21}cos\beta}{n_{21}^2 cos\beta+\sqrt{n_{21}^2-sin^2\beta}} \\ t_Y = \frac{2cos\beta sin\gamma}{sin(\beta+\gamma)} = \frac{2cos\beta}{cos\beta+\sqrt{n_{21}^2-sin^2\beta}} \end{cases}, \tag{2}$$

where $n_{21} = n_2/n_1$, and then power transmission coefficients of polarization states X and Y can be obtained in the following

$$\begin{cases} T_X = \frac{n_2 cos\gamma}{n_1 cos\beta}|t_X|^2 \\ T_Y = \frac{n_2 cos\gamma}{n_1 cos\beta}|t_Y|^2 \end{cases}. \tag{3}$$

Using the parameters above, the received power I can be calculated by the power portions I_X and I_Y of two polarization states

$$I = I_X T_X + I_Y T_Y. \tag{4}$$

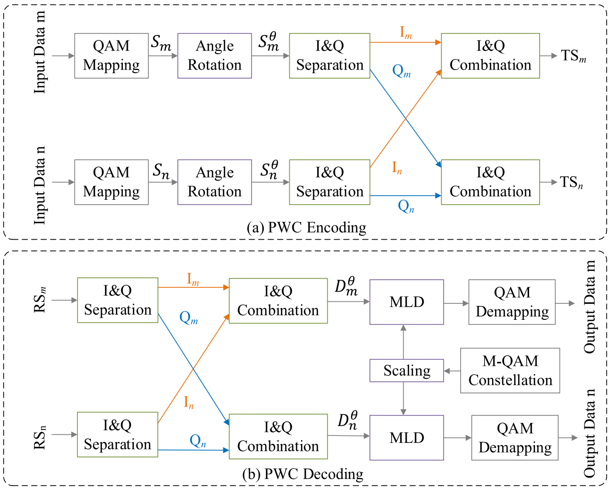

Fig. 2. Illustration pairwise (a) encoding and (b) decoding.

After N times interaction with bubbles, the received optical power is given by

$$I = \sum_{i=1}^{N} I_i = I_X \prod_{i=1}^{N} T_X(\beta_i) + I_Y \prod_{i=1}^{N} T_Y(\beta_i). \tag{5}$$

According to the formula, the instantaneous received power of the two polarized light beams will be different due to the bubble perturbation. Therefore, the received SNR also varies.

C. Principle of Pairwise Coding (PWC)

1) PWC Encoding: The structure of the encoding process of PWC is shown in Fig. 2(a). Firstly, for both PWC schemes, two serial input bits carried on a pair of subcarriers are mapped into M-QAM complex symbols, denoted as

$$\begin{cases} S_m = a_m + b_m j \\ S_n = a_n + b_n j \end{cases}. \tag{6}$$

Then a constant phase shift is applied on each QAM symbol to increase the minimum Euclidean distance between different constellation points [31]. For most cases, the optimal degree is set to be 45° [22], [32]. Paired symbols after rotation can be denoted as

$$\begin{cases} S_m^\theta = S_m e^{j\theta} = a_m \cos\theta - b_m \sin\theta + (a_m \sin\theta + b_m \cos\theta)j \\ S_n^\theta = S_n e^{j\theta} = a_n \cos\theta - b_n \sin\theta + (a_n \sin\theta + b_n \cos\theta)j \end{cases}, \tag{7}$$

Then in-phase (I) and quadrature (Q) interleaving is applied to the rotated symbols in each scheme [33]

$$\begin{cases} TS_m = \Im\left(S_m^\theta\right) + j\Im\left(S_n^\theta\right) \\ \quad\quad = a_m \sin\theta + b_m \cos\theta + (a_n \sin\theta + b_n \cos\theta)j \\ TS_n = \Re\left(S_m^\theta\right) + j\Re\left(S_n^\theta\right) \\ \quad\quad = a_m \cos\theta - b_m \sin\theta + (a_n \cos\theta - b_n \sin\theta)j \end{cases}, \tag{8}$$

where $\Re(.)$ and $\Im(.)$ denote to extract the real and imaginary parts of the complex input, respectively.

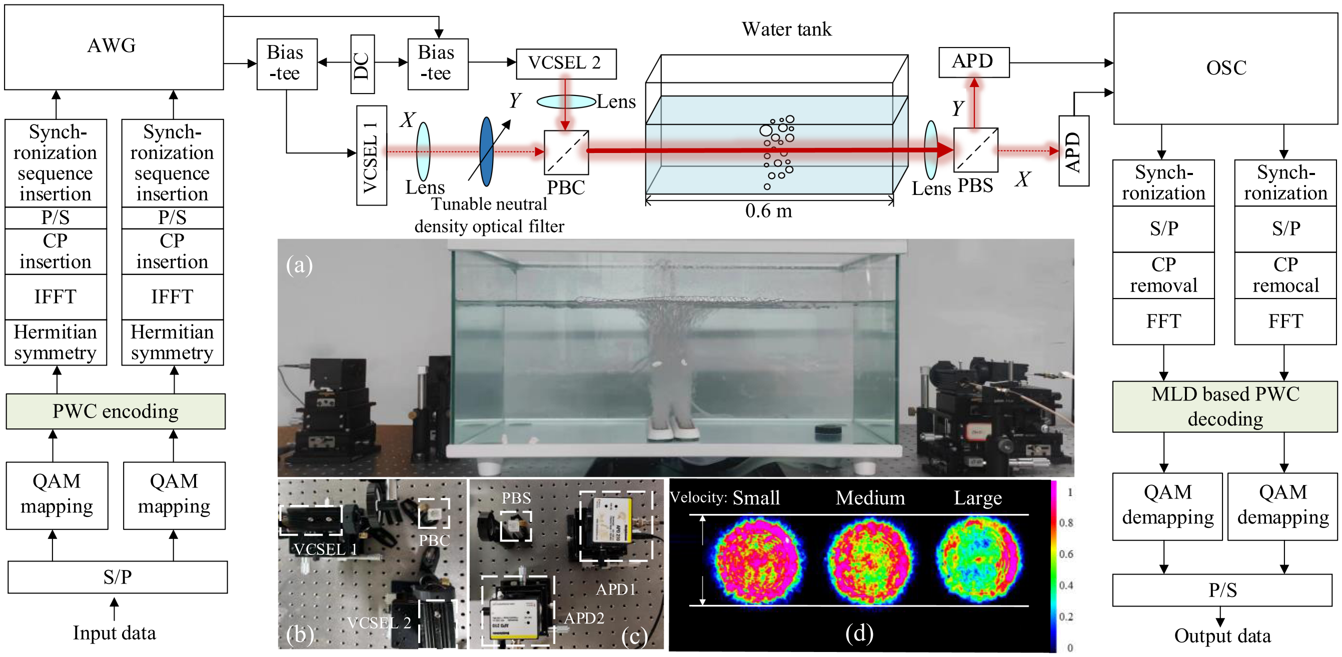

Fig. 3. Schematic of the experimental setup for the PWC-based PolMux-OFDM UOWC system, insert: (a) Overall system setup, (b) transmitter, (c) receiver and (d) distorted received beams with different bubble scenarios.

To deal with the frequency selective fading, the SC-PWC pairing is set to be $(X_m, X_n) = (X_i, X_{N_d-i+1}), i \in N_d$, assuming that the number of data subcarrier N_d is even.

For SCH-PWC, pairwise coding is utilized to compensate SNR difference between two PolMux subchannels. The bubble-induced turbulence channel may cause different refraction and reflection effects on the light beams with different orthogonal polarization states X and Y, which will be analyzed in detail in the next section. Therefore, for SCH-PWC, the subcarriers with the same index from two PolMux subchannels are paired as: $(S_m, S_n) = (S_X, S_Y)$. Then, PWC can be performed with respect to those subchannel pairs, including phase rotation and I/Q component interleaving.

2) PWC Decoding: The SC-PWC and SCH-PWC decoding process is presented in Fig. 2(b). Firstly, the I/Q deinterleaving is employed in paired SCs and subchannels. Similar to the interleaving operation, the I/Q components of Rx *m* and Rx *n* are exchanged. Then MLD is used to detect the signals. Reference constellation is generated by scaling a standard *M*-QAM constellation according to the channel coefficients, which can be expressed as:

$$D_s = \underset{\widehat{\alpha}_i \in \widehat{Q}}{\arg\min} \left\{ \left\| D_i^{\theta} - \widehat{\alpha}_i \right\| \right\} \tag{9}$$

where $||\cdot||$ denotes the Frobenius norm. The scaled *M*-QAM constellation $\hat{\alpha}$,which is an element of the constellation alphabet $\hat{Q}$, is given by:

$$\begin{cases} \hat{\alpha}_m = h_m R\left[\alpha\right] + j h_m R\left[\alpha\right] \\ \hat{\alpha}_n = h_n I\left[\alpha\right] + j h_n I\left[\alpha\right] \end{cases} \tag{10}$$

where h_1 and h_2 represent the channel coefficients of Rx 1 and Rx 2, respectively. *R*[·] and *I*[·] represent the operations to extract the real and imaginary parts, respectively. α is an *M* × 1 vector of standard *M*-QAM constellation. After the PWC decoding process, the output data can be generated through QAM demapping. The decoding process of SCH-PWC and SC-PWC is basically the same, except that the deinterleaving should be performed according to the interleaving pairs.

III. EXPERIMENTAL RESULTS AND DISCUSSIONS

A. *Experimental Setup*

The experimental setup for the PolMux-UOWC system is illustrated in Fig. 3. At the Tx, two random serial bits are generated and converted into parallel streams and are performed with 16-QAM bit-to-symbol mapping. Two different PWC encoding schemes are applied to complex symbols for each bubble condition. Then DCO-OFDM modulation is accomplished by adding pilots, Hermitian symmetry, inverse fast Fourier transform (IFFT), cyclic prefix (CP) insertion, and parallel-to-serial (P/S) conversion. The two series of generated data by MATLAB 2020A DSP steps mentioned before are loaded into the arbitrary waveform generator (AWG, AWG7000A, Tektronix). A bias-tee (ZFBT-6GW+, Mini-circuit) combines the high-frequency data with direct current (DC) components. Two output signals are then transmitted via two transistor outline (TO)-packaged red VCSELs (VCSELs, DV0680M, DERAY) with peak wavelength at 680 nm and combined by a PBC. Two pairs of plano-convex lenses are used on both Tx and Rx to collimate and focus two paths of orthogonally polarized light. A water tank in dimension 0.2 m × 0.3 m × 0.6 m filled with fresh tap water with a bubble generator is utilized as the transmission channel. At the Rx,

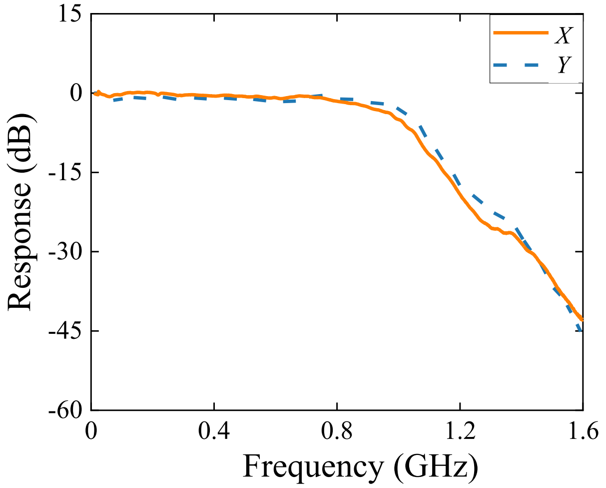

Fig. 4. Frequency response of the PolMux-UOWC system.

a PBS is used at the receiver to separate X and Y light. And two APDs, (APD210, Menlo Systems, 1 GHz)) are utilized to achieve optical-electrical conversion. Then two signals are detected by different channels of a real-time oscilloscope (OSC, MSO73304DX, Tektronix) simultaneously with a sampling rate of 25 GSa/s. Moreover, the frequency response of the whole system is measured by a PNA Network Analyzer (N5227A, Keysight).

B. Bubble-Induced Channel Characterization

In order to introduce the bubble-induced turbulence in the experiments, a bubble generator shown in Fig. 3(a) is used to realize and control the laboratory-simulated bubble channels. It consists of a regulating valve, an air pump, and two 0.07×0.25 m bubble discs. The flow rate of the bubbles generated by the bubble discs can be controlled by adjusting the regulating valve. Four different bubble flow rates: small, medium, large, and ultra-large, are mainly set corresponding to bubble flow rates: 0.39, 0.52, 0.63, and 0.70 *L/s*. Besides, thickness of bubble-effected region can be controlled by the number of bubble disks: 0.07 m with one bubble disc and 0.14 m with two bubble discs. The later demonstrated experimental results are always obtained using two bubble discs (0.14 m) if without thickness statement. Fig. 3(d) presents the captured Gaussian beams of the emitted beam with a diameter of 8.96 mm at three different bubble flow rates obtained by a charge-coupled device (CCD) camera. It can be clearly seen that the beam distortion caused by the bubbles becomes more severe as the rate of the bubbles increases.

As presented in Fig. 4, the -3 dB bandwidths of polarization states X and Y are 0.998 GHz and 0.955 GHz, respectively; the -6 dB bandwidths of polarization states X and Y are 1.022 GHz and 1.068 GHz, respectively. It is obvious that the bandwidth of the system is limited, and the system response is frequency-selective, i.e., the frequency response is monotonically reduced with the increase of frequency. This phenomenon is mainly caused by the APD at Rx, which has a -3 dB bandwidth of about 1 GHz. In addition, in order to achieve a higher transmission data rate, a higher signal bandwidth is needed. Two AWG sampling rates, 1.20 and 4.50 GSa/s are applied with signal bandwidth changes from 0.30 to 1.12 GHz. The estimated SNRs of the received signal under two AWG sampling rates are shown in Fig. 5(a) and (b). The increasing data rate makes the SNR gap change from 5 dB to 10 dB, indicating a more severe frequency selective fading. The response degraded at higher frequency will impact the overall communication performance. Therefore, SC-PWC is demonstrated in this work to address this issue. For the ideal PolMux system, the channel of both polarization states should be constant and time-invariant. However, as analyzed before, the instantaneous received power of two light beams is different because of bubble-induced turbulence, reflecting a time-varying degree of fading on each channel. This kind of phenomenon can be clearly verified in Fig. 6, demonstrating the received waveforms of two PolMux channels from the oscilloscope. When the same square wave is generated at the transmitter, the waveform amplitude at the receiver simultaneously is different results from the refraction and reflection of bubble media. Also, the received optical power is measured when applying different flow rates of bubbles as shown in Fig. 7. The average received optical power values for ultra-large, large, medium, small bubble flow rates were measured to be: 0.157 mW ($\sigma_I^2 = 0.77$), 0.212 mW ($\sigma_I^2 = 0.70$), 0.358 mW ($\sigma_I^2 = 0.13$) and 0.404 mW ($\sigma_I^2 = 0.11$), compared with the result without bubbles: 0.55 mW, corresponding to average percent of intensity attenuations of 71%, 61%, 35%, and 27%, respectively. On the other hand, As the bubble flow rate increases, the received signal experiences more severe fluctuations, which can be reflected by σ_I^2. This mainly results from bubbles in the water move faster, and the density of bubbles increases with higher water pressure, which directly increase contacts between the propagated light and bubbles, leading to a more random optical signal transmission along the path.

C. Received Signal Characterization

Experiments are demonstrated to investigate the effect of different bubble flow rates and locations to the received signals in the communication link. According to the analysis above, the interference of the bubble channel on both signals is random. Therefore, for the same bubble condition, 100 samples under six bubble scenarios with 0.14 m thickness are collected for statistical analysis. Firstly, Fig. 8 presents the SNR results with AWG sampling rate fixed to 4.50 GSa/s, and the oscilloscope samples at a rate of 25 GSa/s to recover the transmitted signal. The size of the IFFT is 512, while the number of data subcarriers is 122 with the QAM modulation order of 16. Considering the employed PolMux system, the overall data rate is the sum of both subchannels: $N_{data}/N \times \log_2^M \times 2 = 8.58\, G/s$. Fig. 8(a)–(c) shows the SNR over SCs of both PolMux signals and their difference (histogram) when the bubble flow rate is small, medium, and large, respectively, with bubble position set in the middle of the VCSEL and APD. Fig. 8(d)–(f) present the SNR results when the bubble rate is ultra-large with bubble position is close to the Tx (0.1 m from the light source, $\sigma_I^2 = 0.84$), in the middle ($\sigma_I^2 = 0.78$) and close to the Rx (0.1 m from

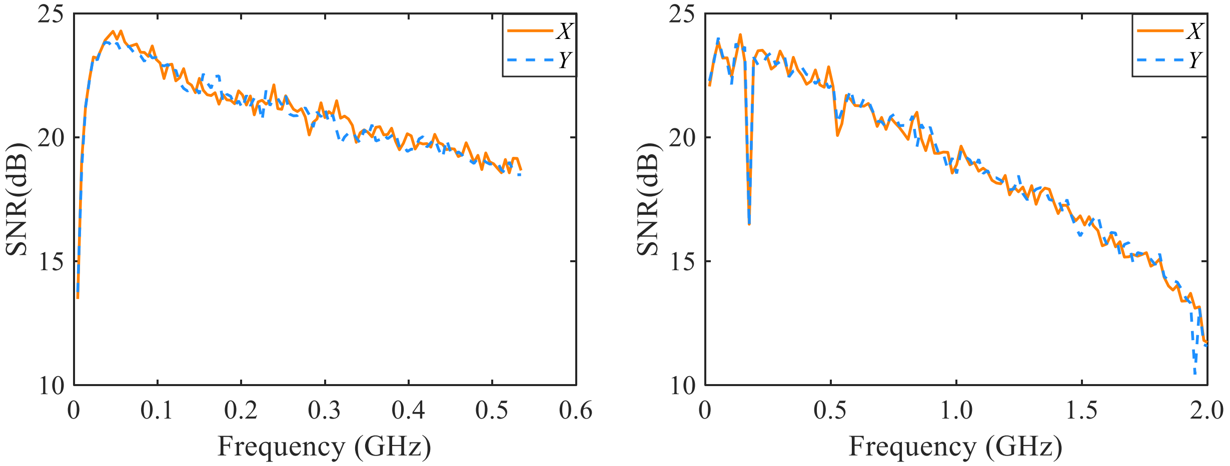

(a) (b)

Fig. 5. SNR distributions of the received polarized signal with AWG sampling rate (a) 1.20 GSa/s and (b) 4.50 GSa/s.

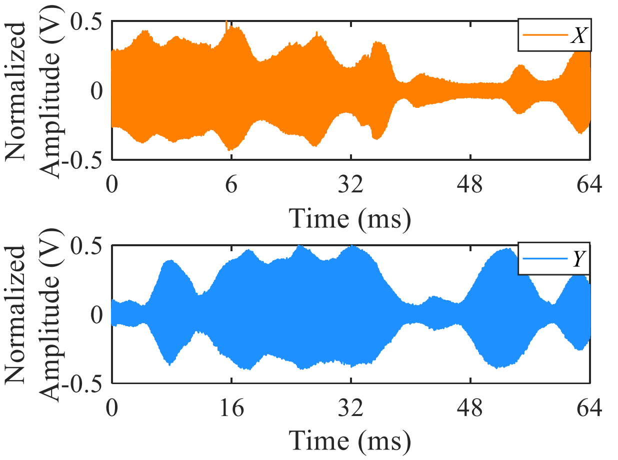

Fig. 6. Normalized received waveforms of polarization state: (a) *X* and (b) *Y*.

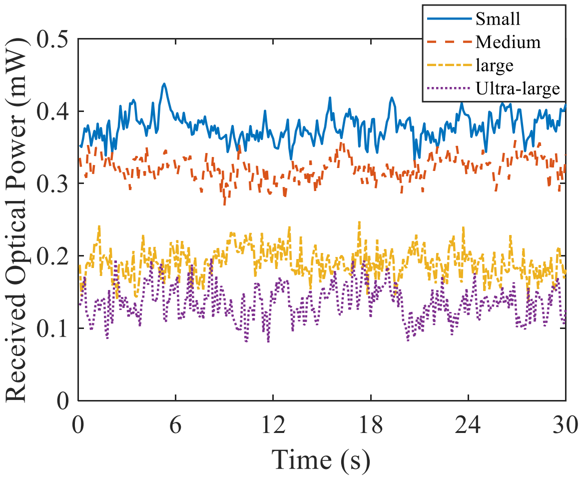

Fig. 7. Receive optical power under different bubble flow rates scenarios.

the APD, $\sigma_I^2 = 0.35$), respectively. Through the observation of 100 samples under five different bubble channels. It can be found that there exists an uncertain SNR difference between two PolMux signals at the same moment and fluctuates with time. With the increase of bubble flow rate, the closer bubble location to the Tx, SNR fluctuation will be more severe and the difference between two subchannels will be more obvious. This phenomenon can be regarded as the SNR imbalance of two PolMux signals caused by bubble-induced turbulence.

To characterize the correlation between received signals from two subchannels, the received SNR results of polarization states *X* and *Y* under six bubble scenarios are presented as scatter diagrams in Fig. 9. According to the obtained correlation coefficient (all less than 0.2) and Pearson correlation law, the correlation between the received signal intensity of *X* and *Y* is negligible. That is, two subchannels are randomly affected by bubbles, and the variation of the receiving intensity of one subchannel does not affect the other. In addition, as shown in the figure, in most cases, when one subchannel confronts with deep fading, the other subchannel can still have a satisfactory SNR. Hence, the probability that both subchannels suffer from deep fading is relatively small, which provides the possibility for compensation by SCH-PWC.

Furthermore, to investigate the SNR imbalance in different bubble cases and make the results more intuitive, the calculated probability density function (PDF) of IOMIOM ΔSNR with different bubble flow rate are presented in Fig. 10(a), and PDF of ΔSNR with different bubble positions with 0.07 and 0.14 m bubble-effected region thickness are demonstrated in Fig. 10(b). The peak of the PDF curve appears at the place with larger ΔSNR when the bubble flow rate is higher or the position is closer to Tx and the distribution of ΔSNR is more expansive. In the meanwhile, according to the comparison of the thickness of the two groups of bubbles with different thickness in Fig. 10(b), with the same bubble flow rate and bubble position, the larger bubble thickness also increases the probability of larger ΔSNR

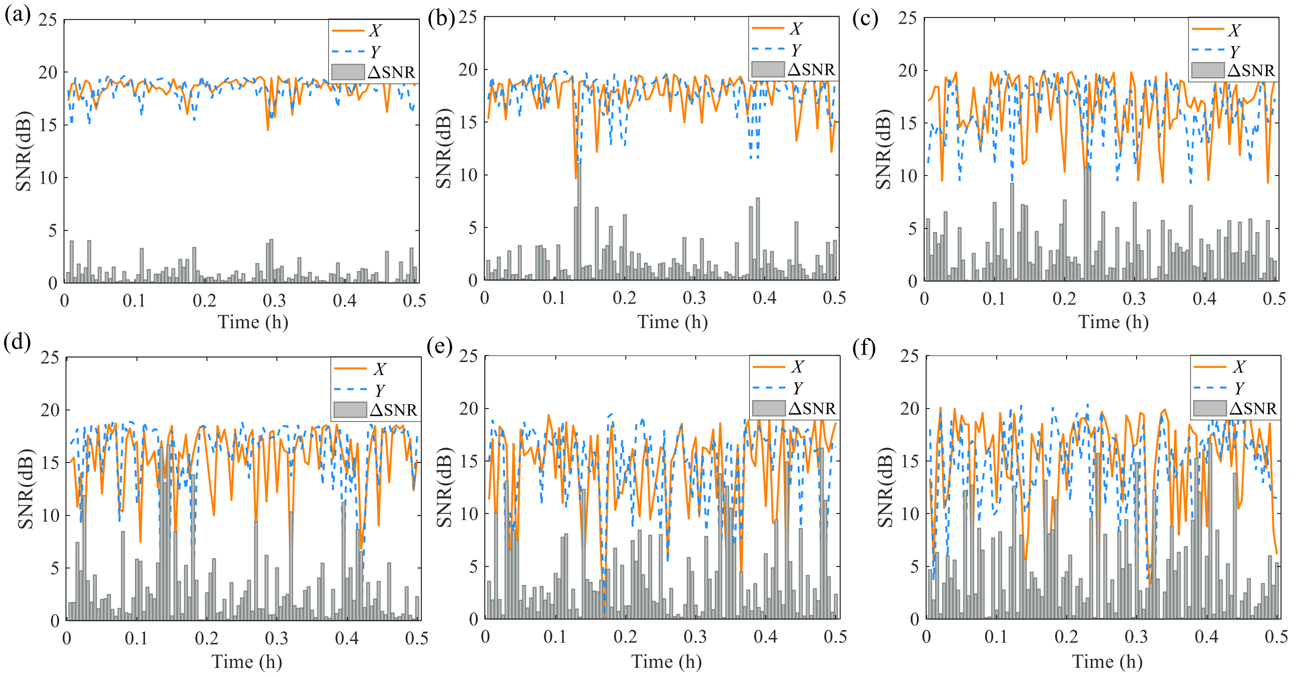

Fig. 8. SNR results of polarization state *X*, *Y* and their difference with collected samples under bubble scenario (flow rate /position): (a) Small/middle, (b) medium/middle, (c) large/middle, (d) ultra-large/Tx side, (e) ultra-large/ middle and (f) ultra-large/Rx side.

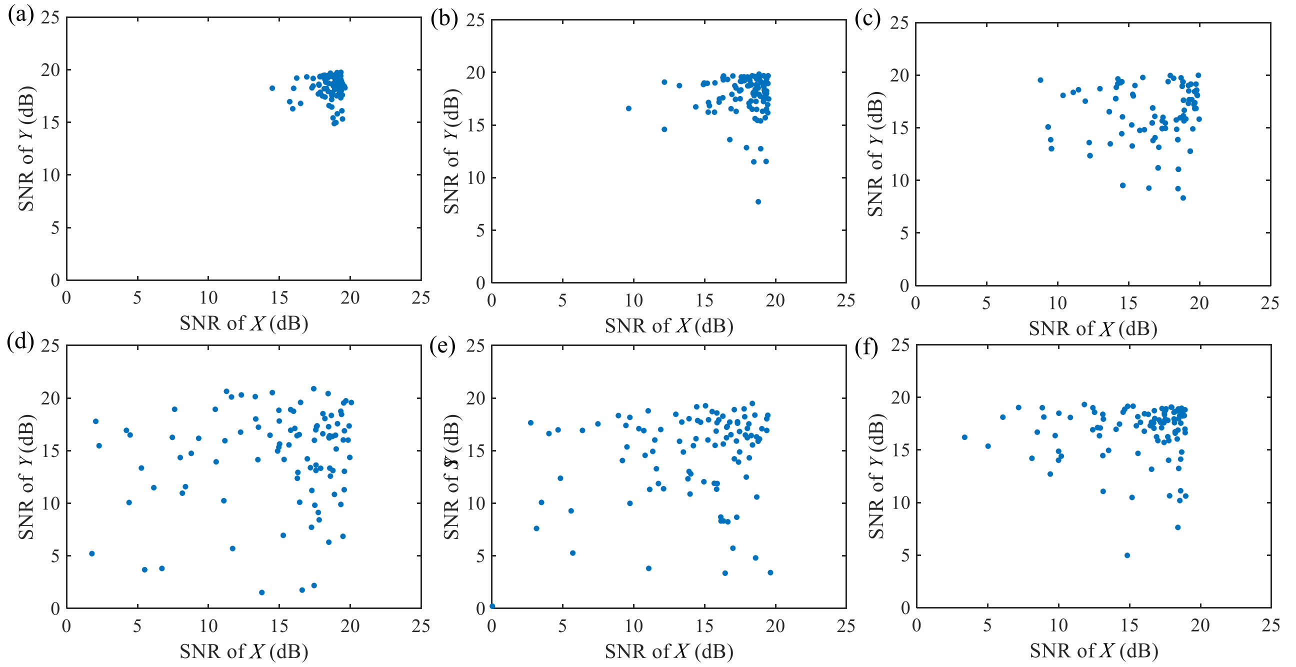

Fig. 9. Measured SNR scatter diagram of polarization states X and Y under different bubble scenarios (flow rate /position): (a) Small/middle, (b) medium/middle, (c) large/middle, (d) ultra-large/Tx side, (e) ultra-large/middle, and (f) ultra-large/Rx side.

and broadens the PDF. This indicates the probability of a more prominent divergence and uncertainty in SNR between the two subchannels in the above cases. The reason is that with the higher bubble flow rate and thickness, or closer the bubble is to Tx, the less probability light beam would enter the APD after interacting with those bubbles. According to the selectivity of refraction generated by the contact surface between light and bubbles to the two polarized light beams mentioned in Section II, the received polarized light signal intensity difference will increase, which causes SNR imbalance to be more pronounced. In conclusion,

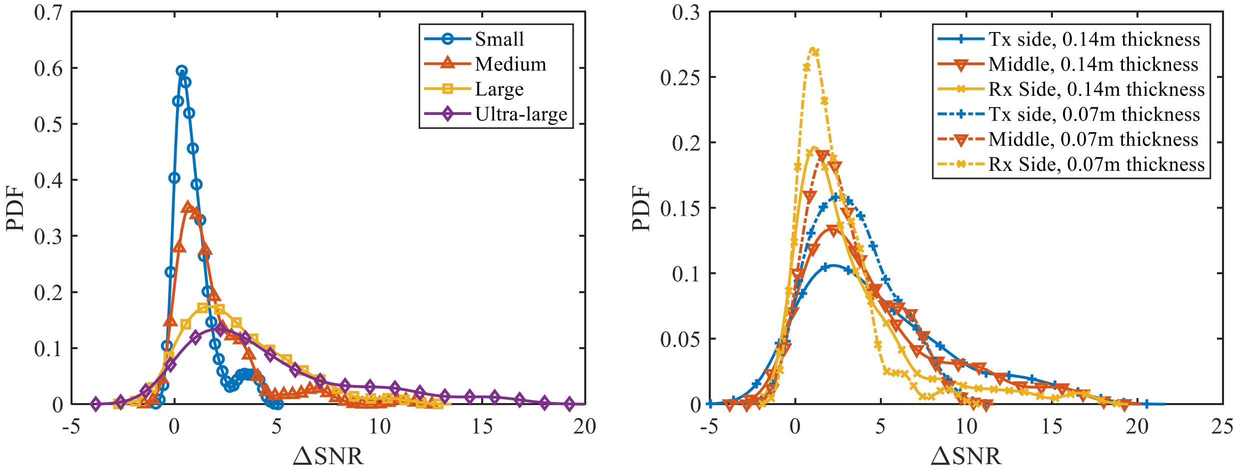

(a) (b)

Fig. 10. PDF of the SNR difference between two orthogonally polarized signals under scenarios: (a) Varying bubble degrees with position fixed at middle and (b) different bubble positions with ultra-large bubble flow rate.

increasing the bubble flow rate, thickness and with bubble position closer to the Tx makes the SNR imbalance problem between the two PolMux subchannels more severe.

IV. PWC TECHNIQUES TO OVERCOME THE BUBBLE-INDUCED TURBULENCE

In this section, the improvement of communication performance by applying PWC schemes in each scenario is investigated. Due to the bandwidth limitation of the light source and photodetector, the frequency response of most optical wireless channels would be confronted with degradation at subcarriers with a higher index. SC-PWC is designed to compensate imbalance SNR of those OFDM SCs. After SC-PWC encoding, the unequal SNRs between two SCs caused by frequency selective fading become the I and Q components of each SC. Therefore, the system performance is maximized by averaging the unequal SNR in those paired SCs. SCH-PWC is proposed to overcome the channel SNR imbalance issue. After SCH-PWC encoding, the SNR difference between subchannels caused by unstable underwater channels can be converted to the difference between I/Q components of each polarization. Thus, the real and imaginary parts of the received symbols are affected by two independent channel fading coefficients. If one channel loses one component due to deep fading, the other component is still valid. This will provide modulation diversity gain, or equivalently, more robust performance against the bubble channel.

Then BER performance of the SC-PWC and SCH-PWC scheme is analyzed as follows. Also, 100 samples are collected, and their cumulative distribution function (CDF) is analyzed for uncoded and PWC schemes facing each bubble scenario with 0.14 m bubble-effected region thickness. CDF results under bubble flow rate: small, medium and large with position fixed at middle is shown in Fig. 11(a)–(c). The frequency response of the channel is shown in Fig. 5(b) with AWG sampling rate fixed at 4.50 GSa/s. The system is significantly affected by frequency selective fading due to high signal bandwidth. Therefore, SC-PWC achieves better overall compensation performance than SCH-PWC as presented in the figure. Besides, with a lower bubble flow rate, there is no significant gain in applying SCH-PWC since the SNR imbalance is not prominent in this case. However, when the flow rate of bubbles gradually increases, the SNR imbalance between subchannels becomes apparent, which makes the compensation of SCH-PWC more significant. CDF results of bubble position close to Tx and Rx with ultra-large bubble flow rate are shown in Fig. 11(d) and (e). As the bubble flow rate increases, the SNR average value decreases, accompanied by an increase in channel SNR imbalance as well as the probability of channel deep fading. In this case, the interleaving of high and low-frequency SCs will, on the other hand, degrade the system performance, which even makes the SC-PWC compensation performance lower than the uncoded scheme. However, the compensation performance of SCH-PWC is better at this moment due to the severe PolMux subchannel SNR imbalance.

In addition, another experiment illustrating the effectiveness of SCH-PWC is demonstrated. While the bubble channel setup is consistent with Fig. 11(c). The SNRs of different SCs are shown in Fig. 5(a), with the AWG sampling rate reduced to 1.20 GSa/s, large bubble flow rate and position fixed at middle. The CDF of BER results is shown in Fig. 11(f). The frequency selective fading problem is alleviated with reduced signal bandwidth. In this case, the BER performance is dominated by the channel SNR imbalance issue. Therefore, SCH-PWC achieves the best compensation performance. These results reflect the superiority of SCH-PWC in bubble-induced PolMux-UOWC channels.

In order to further verify the improvement of communication performance provided by different coding schemes, the outage probability is calculated for all the channel conditions shown in Table I. SC-PWC has a relatively lower outage probability when the sampling rate is higher under all bubble conditions. The outage probability can be reduced to one-third of the uncoded case with a small bubble flow rate compared with half when the bubble flow rate is medium and large. When the sampling

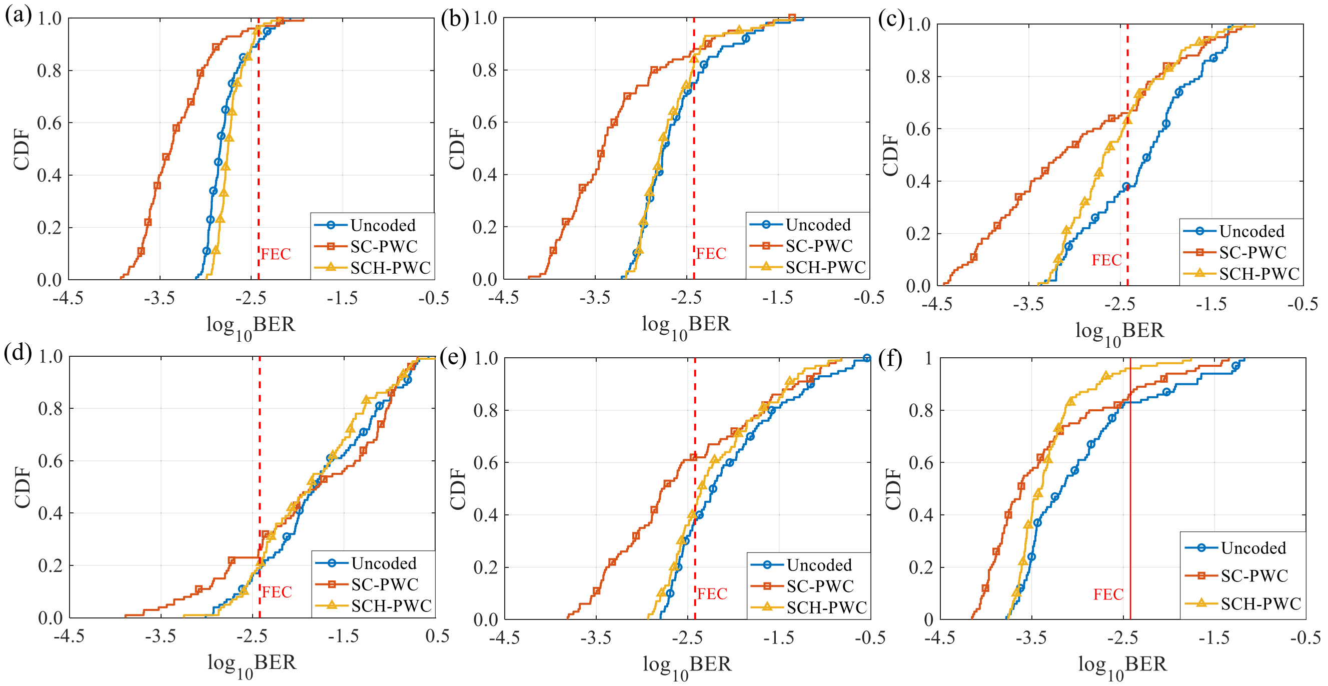

Fig. 11. CDF of measured BERs with (a) AWG sampling rate 4.50 GSa/s, small bubble flow rate, position at middle, (b) AWG sampling rate 4.50 GSa/s, medium bubble flow rate, position at middle, (c) AWG sampling rate 4.50 GSa/s, large bubble flow rate, position at middle, (d) AWG sampling rate 4.50 GSa/s, ultra-large bubble flow rate, position close to Tx side, (e) AWG sampling rate 4.50 GSa/s, ultra-large bubble flow rate, position close to Rx side and (f) AWG sampling rate 1.20 GSa/s, large bubble flow rate, position at middle.

TABLE I
OUTAGE PROBABILITY OF DIFFERENT SCHEMES UNDER DIFFERENT AWG SAMPLING RATES AND BUBBLE SCENARIOS

AWG Sampling Rate (GSa/s)	Bubble Scenario (Flow rate /Position)	Uncoded	SC-PWC	SCH-PWC
4.5	Small/Middle	9%	4%	3%
	Medium/Middle	25%	12%	17%
	Large/Middle	62%	34%	37%
	Ultra-large /Tx side	81%	74%	80%
	Ultra-large /Rx side	62%	38%	58%
1.2	Large/Middle	17%	14%	4%

rate is reduced to 1.20 GSa/s, SCH-PWC achieves the best performance with the outage probability reduced from 17% to 4% when the bubble flow rate is large. These results also confirm the measured CDF of BER. Besides, we use collected samples to calculate the average value of BER with and without coding under different bubble channel conditions. Taking the large bubble flow rate as an example, the average BER for the uncoded case is 1.22×10^{-2}, while SC-PWC and SCH-PWC are $6.92 \times 10^{-3}$and 6.80×10^{-3}, respectively, resulting in overall BER performance improved by nearly 50%.

The BER corresponding to different subcarrier indexes calculated by the superposition of collected samples when the bubble flow rate is large is shown in Fig. 12. Without coding, the BER performance at high frequencies degraded due to the system bandwidth limitation. For SC-PWC, the performance of BER in the high index has been significantly improved due to the benefit of pairing with low-frequency SCs. At the expense of errors occurring in lower frequency SCs, the BER of nearly 90% of the SCs in the SC-PWC scheme is acceptable with forward error correction (FEC) criteria range: 3.8×10^{-3}, compared with the BER of nearly half of the SCs exceeding the FEC limit for the uncoded case. As for SCH-PWC, with the SNR imbalance problem alleviated by interleaving two channels, the BERs of all SCs are smaller than the uncoded case.

In general, both PWC schemes achieve the overall compensation at a low computational cost. For SC-PWC, the compensation performance is ideal when the system bandwidth is severely limited, or the bubble flow rate is small. However, when the flow rate of bubbles becomes larger, accompanied by decreasing in the SNR average value, interleaving of high and low-frequency

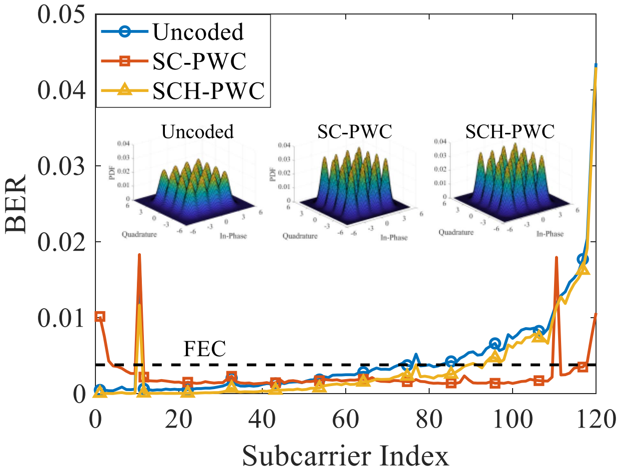

Fig. 12. BER versus subcarrier index of different schemes, inset: Associated distribution of constellation plots.

SCs will, on the other hand, degrade compensation performance. As for another, SCH-PWC achieves better compensation performance with severe channel SNR imbalance, especially with a smaller SNR gap. Thus, it can realize more stable communication performance under the bubble-induced turbulence channel. The associated distribution of 16-QAM constellation diagrams shown in inserted Fig. 11 for the received uncoded and coded signals after I/Q deinterleaving. As expected, the constellation points of the received PWC deinterleaved signals are more concentrated, which benefits the subsequent QAM demodulation.

V. CONCLUSION

We have experimentally demonstrated a more stable 8.58 Gbps PolMux-UOWC system under different bubble scenarios. Three different bubble flow rates, typical bubble positions and bubble-effected region thicknesses were performed to simulate the impairments brought by various bubble scenarios in the ocean. The bubble-induced turbulence channel affects two orthogonal polarized PolMux signals to various extents, which are reflected in the SNR imbalance between the two subchannels. Furthermore, we propose to exploit SCH-PWC in the PolMux-UOWC system to address the two subchannel SNR imbalance issue, while using SC-PWC to solve the frequency selective fading caused by system bandwidth limitation. Last but not least, the appropriate selection of coding schemes under different bubble conditions has been summarized. This work provides the first comprehensive investigation for implementing PolMux systems to underwater transmission in the presence of air bubbles and demonstrates a practical solution for bubble-induced impairments. Our future work will mainly focus on bubble channel modeling and the design of more advanced coding schemes for the PolMux transmission under turbulent channels.

REFERENCES

[1] S. Arnon, "Underwater optical wireless communication network," *Proc. SPIE*, vol. 49, no. 1, 2010, Art. no. 015001.

[2] Z. Wei, Z. Wang, J. Zhang, Q. Li, J. Zhang, and H. Y. Fu, "Evolution of optical wireless communication for B5G/6G," *Prog. Quantum Electron.*, vol. 83, May 2022, Art. no. 100398, doi: 10.1016/j.pquantelec.2022.100398.

[3] Z. Zeng, S. Fu, H. Zhang, Y. Dong, and J. Cheng, "A survey of underwater optical wireless communications," *IEEE Commun. Surv. Tut.*, vol. 19, no. 1, pp. 204–238, Firstquarter 2017.

[4] P. Chvojka et al., "Visible light communications: Increasing data rates with polarization division multiplexing," *Opt. Lett.*, vol. 45, no. 11, pp. 2977–2980, 2020.

[5] A. Trichili, K.-H. Park, M. Zghal, B. S. Ooi, and M.-S. Alouini, "Communicating using spatial mode multiplexing: Potentials, challenges, and perspectives," *IEEE Commun. Surv. Tut.*, vol. 21, no. 4, pp. 3175–3203, Fourthquarter 2019.

[6] X. Zhou et al., "64-Tb/s, 8 b/s/Hz, PDM-36QAM transmission over 320 km using both pre-and post-transmission digital signal processing," *J. Lightw. Technol.*, vol. 29, no. 4, pp. 571–577, Feb. 2011.

[7] T. Richter et al., "Transmission of single-channel 16-QAM data signals at terabaud symbol rates," *J. Lightw. Technol.*, vol. 30, no. 4, pp. 504–511, Feb. 2012.

[8] C. Yeh, H. Chen, Y. Liu, and C. W. Chow, "Polarization-multiplexed 2×2 phosphor-LED wireless light communication without using analog equalization and optical blue filter," *Opt. Commun.*, vol. 334, pp. 8–11, 2015.

[9] L. Zhang et al., "Towards a 20 Gbps multi-user bubble turbulent NOMA UOWC system with green and blue polarization multiplexing," *Opt. Exp.*, vol. 28, no. 21, pp. 31796–31807, 2020.

[10] J. Miller et al., "Underwater optical communication link using polarization division multiplexing and orbital angular momentum multiplexing," in *Proc. OCEANS Anchorage*, 2017, pp. 1–4.

[11] H. Elgala, R. Mesleh, and H. Haas, "Indoor optical wireless communication: Potential and state-of-the-art," *IEEE Commun. Mag.*, vol. 49, no. 9, pp. 56–62, Sep. 2011.

[12] C. S. Park and K. B. Lee, "Transmit power allocation for BER performance improvement in multicarrier systems," *IEEE Trans. Commun.*, vol. 52, no. 10, pp. 1658–1663, Oct. 2004.

[13] B. S. Krongold, K. Ramchandran, and D. L. Jones, "Computationally efficient optimal power allocation algorithm for multicarrier communication systems," in *Proc. IEEE Int. Conf. Commun. Conf. Rec. Affiliated SUPERCOMM*, 1998, vol. 2, pp. 1018–1022.

[14] J. A. Simpson, B. L. Hughes, and J. F. Muth, "A spatial diversity system to measure optical fading in an underwater communications channel," in *Proc. IEEE OCEANS Conf.*, 2009, pp. 1–6.

[15] H. M. Oubei et al., "Simple statistical channel model for weak temperature-induced turbulence in underwater wireless optical communication systems," *Opt. Lett.*, vol. 42, no. 13, pp. 2455–2458, 2017.

[16] H. M. Oubei, R. T. ElAfandy, K.-H. Park, T. K. Ng, M.-S. Alouini, and B. S. Ooi, "Performance evaluation of underwater wireless optical communications links in the presence of different air bubble populations," *IEEE Photon. J.*, vol. 9, no. 2, Apr. 2017, Art. no. 7903009.

[17] M. V. Jamali et al., "Statistical studies of fading in underwater wireless optical channels in the presence of air bubble, temperature, and salinity random variations," *IEEE Trans. Commun.*, vol. 66, no. 10, pp. 4706–4723, Oct. 2018.

[18] D. Stramski, E. Boss, D. Bogucki, and K. J. Voss, "The role of seawater constituents in light backscattering in the ocean," *Prog. Oceanogr.*, vol. 61, no. 1, pp. 27–56, 2004.

[19] E. T. Baker and J. W. Lavelle, "The effect of particle size on the light attenuation coefficient of natural suspensions," *J. Geophys. Res.: Oceans*, vol. 89, no. C5, pp. 8197–8203, 1984.

[20] S.-J. Kim, D.-H. Kwon, S.-H. Yang, and S.-K. Han, "Asymmetric multi-input multi-output system in visible light communication for polarization-tolerant polarization division multiplexing transmission," *Proc. SPIE*, vol. 55, no. 3, 2016, Art. no. 036102.

[21] Y. Zhang, Y. Wang, A. Huang, and X. Hu, "Effect of underwater suspended particles on the transmission characteristics of polarized lasers," *J. Opt. Soc. Amer. A*, vol. 36, no. 1, pp. 61–70, 2019.

[22] J. Boutros and E. Viterbo, "Signal space diversity: A power-and bandwidth-efficient diversity technique for the Rayleigh fading channel," *IEEE Trans. Inf. Theory*, vol. 44, no. 4, pp. 1453–1467, Jul. 1998.

[23] C. Zhu, B. Song, B. Corcoran, L. Zhuang, and A. J. Lowery, "Improved polarization dependent loss tolerance for polarization multiplexed coherent optical systems by polarization pairwise coding," *Opt. Exp.*, vol. 23, no. 21, pp. 27434–27447, 2015.

[24] B. Song, B. Corcoran, Q. Wang, L. Zhuang, and A. J. Lowery, "Subcarrier pairwise coding for short-haul L/E-ACO-OFDM," *IEEE Photon. Technol. Lett.*, vol. 29, no. 18, pp. 1584–1587, Sep. 2017.

[25] I. N. Osahon, C. Ziyan, T. Adiono, and W. O. Popoola, “SI-POF transmission with OFDM and sub-carrier pairwise coding,” in *Proc. IEEE Int. Federation Inf. Process. Int. Conf. Perform. Eval. Model. Wired Wireless Netw.*, 2018, pp. 1–5.

[26] H. G. Olanrewaju, J. Thompson, and W. O. Popoola, “Pairwise coding for MIMO-OFDM visible light communication,” *IEEE Trans. Wireless Commun.*, vol. 19, no. 2, pp. 1210–1220, Feb. 2020.

[27] J. M. Ostermann, P. Debernardi, and R. Michalzik, “Surface-grating VCSELs with dynamically stable light output polarization,” *IEEE Photon. Technol. Lett.*, vol. 17, no. 12, pp. 2505–2507, Dec. 2005.

[28] C. Fuchs et al., “Spatiotemporal turn-on dynamics of grating relief VCSELs,” *IEEE J. Quantum Electron.*, vol. 43, no. 12, pp. 1227–1234, Dec. 2007.

[29] L. C. Andrews, R. L. Phillips, C. Y. Hopen, and M. Al-Habash, “Theory of optical scintillation,” *J. Opt. Soc. Amer. A*, vol. 16, no. 6, pp. 1417–1429, 1999.

[30] H. Wang, Y. Wang, S. Chen, Y. Qi, and H. Liu, “Research on polarization of water and bubble scattering echo,” *Proc. SPIE*, vol. 8192, 2011, pp. 168–175.

[31] S. K. Mohammed, E. Viterbo, Y. Hong, and A. Chockalingam, “MIMO precoding with X-and Y-codes,” *IEEE Trans. Inf. Theory*, vol. 57, no. 6, pp. 3542–3566, Jun. 2011.

[32] S. Özyurt, O. Kucur, and İ. Altunbaş, “Error performance of rotated phase shift keying modulation over fading channels,” *Wireless Pers. Commun.*, vol. 43, no. 4, pp. 1453–1463, Dec. 2007, doi: 10.1007/s11277-007-9319-7.

[33] G. Taricco and E. Viterbo, “Performance of component interleaved signal sets for fading channels,” *Electron. Lett.*, vol. 32, no. 13, pp. 1170–1172, 1996.

Bohua Deng received the B.E. degree in information engineering from Xi’an Jiaotong University, Xi’an, China, in 2021. She is currently working toward the M.E. degree in data science and information technology with Tsinghua University, Beijing, China. Her research interests include optical communication and networking, and optical signal processing.

Jiwei Wang received the B.E. degree in electronic and information engineering from the Inner Mongolia University of Science and Technology, Baotou, China, in 2021. He is currently working toward the M.E. degree in information and communication engineering with Chongqing University, Chongqing, China. His research interests include optical wireless communication and optical signal processing.

Zhaoming Wang received the B.S. degree from the East China University of Science and Technology, Shanghai, China, in 2019, and the M.S. degrees in data science and information technology from Tsinghua University, Beijing, China, in 2022. He is currently working toward the D.Phil. degree with the Department of Engineering Science, University of Oxford, Oxford, U.K. His research interests include optical wireless communication, beam steering, and novel photoelectric device.

Zeyad A. H. Qasem (Student Member, IEEE) received the Ph.D. degree in communication and information systems from the School of Informatics, Xiamen University, Xiamen, China, in 2021. He is currently a Postdoctoral Fellow with Peking University, Shenzhen, China. His research interests include wireless networks, signal processing, and underwater communications.

Qian Li (Senior Member, IEEE) received the Bachelor of Science degree from Zhejiang University, Hangzhou, China, in 2003, the Master of Science degree from the Royal Institute of Technology (KTH), Stockholm, Sweden, in 2005, and the Ph.D. degree from the Hong Kong Polytechnic University, Hong Kong, in 2009. After graduation, she was a Visiting Scholar with the University of Washington, Seattle, WA, USA, and a Postdoctoral Fellow with the Hong Kong Polytechnic University. In 2012, she joined the School of Electronic and Computer Engineering (ECE), Peking University, Beijing, China, as an Assistant Professor. Since 2013, she has been an Associate Professor with ECE. Her research interests include nonlinear optics, ultrafast optics, and integrated optics. Dr. Li is a Senior Member of the Optical Society of America. From March 2017 to April 2019, she is the Vice Chair of IEEE ED/SSC Beijing Section, Shenzhen Chapter and the Chair of EDS. Since 2015, she has been an Advisor of OSA Student Chapter in Peking University Shenzhen Graduate School. Since 2019, she has also been an Advisor of Peking University Shenzhen Graduate School IEEE Photonics Society Student Branch Chapter.

Xinke Tang biography not available at the time of publication.

Chen Chen (Member, IEEE) received the B.S. and M.Eng. degrees from the University of Electronic Science and Technology of China, Chengdu, China, in 2010 and 2013, respectively, and the Ph.D. degree from Nanyang Technological University, Singapore, in 2017. From 2017 to 2019, he was a Postdoctoral Researcher with the School of Electrical and Electronic Engineering, Nanyang Technological University. He is currently a Research Professor with the School of Microelectronics and Communication Engineering, Chongqing University, Chongqing, China. His research interests include optical wireless communication, optical access networks, Internet of Things, and machine learning.

H. Y. Fu (Senior Member, IEEE) received the B.S. degree in electronic and information engineering from Zhejiang University, Hangzhou, China, and the M.S. degree in electrical engineering with specialty in photonics from the Royal Institute of Technology, Stockholm, Sweden, and the Ph.D. degree from the Department of Electrical Engineering, Hong Kong Polytechnic University, Hong Kong. He is currently a tenured-Associate Professor of Tsinghua Shenzhen International Graduate School (SIGS), Tsinghua University, Beijing, China From 2005 to 2010, he was a Research Assistant and then Research Associate with Photonic Research Center, the Hong Kong Polytechnic University. From 2010 to April 2017, he was a founding Member and leading the advanced fiber optic communications research with Central Research Institute, Huawei. He was a Project Manager of All-Optical Networks (AON), which was evolved to a company-wide flagship research project that covers whole aspects of next generation optical communication technologies to guarantee Huawei’s leading position. He has authored or coauthored more than 280 journal or conference papers, three book chapters, more than 80 grant/pending China /Europe/Japan/ U.S. patents. His research interests include integrated photonics and its related applications, fiber optical communications, and fiber optical sensing technologies. He was also a representative for Huawei at several industry/academic standards/forums. From 2012 to 2013, he was an active Contributor at IEEE 802.3 Ethernet and Optical Internetworking Forum (OIF), where he was an OIF Speaker. Dr. Fu is a Life Member of OSA and SPIE. Since 2017, he has been an Advisor of OSA Student Chapter at TBSI, Tsinghua University. Since 2020, he has also been an Advisor of IEEE Photonics Society Student Branch Chapter and SPIE Student Chapter at Tsinghua SIGS.